arXiv:1304.4387v2 [physics.ao-ph] 23 Apr 2013

Lagrangian transport in a microtidal coastal area: the Bay of Palma, Mallorca Island, Spain

Ismael Hernández-Carrasco[1*], Cristóbal López[1],
Alejandro Orfila[2] and Emilio Hernández-García[1]

[1]Instituto de Física Interdisciplinar y Sistemas Complejos (CSIC-UIB)
07122 Palma de Mallorca, Spain
[2]IMEDEA, Instituto Mediterráneo de Estudios Avanzados (CSIC-UIB)
07190 Esporles, Spain

[*]To whom correspondence should be addressed; E-mail: ismael@ifisc.uib.es

Abstract

Coastal transport in the Bay of Palma, a small region in the island of Mallorca, Spain, is characterized in terms of Lagrangian descriptors. The data sets used for this study are the output for two months of a high resolution realistic numerical model, ROMS, forced atmospherically and with a spatial resolution of 300 m. Semi-persistent Lagrangian coherent structures (LCS) are found during both months. We study the fluid interchange between the Bay and the open ocean by computing particle trajectories and residence times. We found clear differences between autumn and summer. Stirring is smaller in autumn (October) than in summer (July), presenting diurnal variability at both months, probably induced by the effect of the wind. The escape rate of particles out of the Bay is qualitatively different, with more particles escaping to the ocean in October than in July. We show that LCSs separate regions with different transport properties, and display spatial distributions of residence times on synoptic Lagrangian maps. Finally, we compare the transport at the bottom layer, strongly influenced by the bottom drag, with surface transport strongly forced by the wind.

1 Introduction

The study of transport and mixing in coastal flows is of major interest because of their economic and ecological importance. Due to the particularities that they present, like influence of complex topography, coastline shape and the direct driving at the surface by highly variable wind forcing, coastal flow dynamics remains still poorly understood.

Recently, coastal observations and modeling efforts in different regions have been addressed from the Lagrangian point of view: [25] showed that Lagrangian Coherent Structures (LCSs) computed from velocity fields obtained from HF Radar measurements can be used to predict pollutant dispersion in the coast of Florida; [13] detected LCSs with HF Radar data in the Gulf of Eliat, Israel, and [18] studied small-scale properties of dispersion measurements obtained from HF Radar data in the Gulf of La Spezia, Italy. Besides Radar measurements, LCSs obtained from velocity data of high resolution numerical models have been used to analyze the effect of the waves on LCS in the Bay of Palma, Spain [12], to study the transport in the tidal flow of Ria de Vigo, Spain [20], or to study the water quality of a very small coastal region, the Hobie Beach, USA [11] Also, data from drifters released in the Santa Barbara Channel were used by [30] to characterize relative dispersion, very useful to improve Lagrangian stochastic models. The application of Lagrangian techniques to study the dynamics in a shallow lake (small closed basin) has been performed in [32].

In this work we study some transport properties in the Bay of Palma using Lagrangian techniques. The Bay is a semi-enclosed basin located in the southwest of the island of Mallorca (western Mediterranean sea), whose coastal flow is strongly induced by the wind, particularly characterized by the presence of persistent sea breeze during the summer months. Forcing by tides is almost negligible with a tidal amplitude of less than $0.25m$. The Lagrangian diagnosis will be obtained from velocity data of a realistic numerical model at high resolution, which resolves spatial scales of a few hundred of meters. We investigate the horizontal transport during two months corresponding to different seasons (autumn and summer) at the sea surface and at the deepest layer, in order to highlight the effect of the wind on transport. We compute the barriers and avenues to transport (LCS) from lines of high values of Finite-Size Lyapunov Exponents (FSLE). We also present calculations of residence times and show synoptic Lagrangian maps (SLM) of these times [26], which will allow us a detailed visualization of the interchange of fluid particles between the Bay and the open sea. As a central point in our study, the relationship between LCSs and areas of different residence times will be analyzed.

The organization of this paper is as follows. The data set used in the computations and the area of study is described in Section 2. Section 3 presents a brief overview of the Lagrangian tools that are used. Before presenting the Lagrangian results, we show in Section 4 a short list of Eulerian results by studying the velocties in the Bay. We show in Section 5 a coastal characterization of stirring of the Bay of Palma in terms of FSLE and residence times. Using the definition of LCS given in Section 3, Lagrangian barriers are identified in the domain of interest. We compute escape rates and residence times of fluid particles to describe the transport relation between the Bay and the open ocean. We provide possible mechanisms to explain differences in the residences times and FSLE between different seasonal months. Finally we summarize the main results in Section 6.

2 Data and characteristics of the study region

2.1 Area of study

The island of Mallorca (Fig. 1) is part of the Balearic Islands Archipelago and is located in the center of the western Mediterranean (between 39° and 40°N and 2.50° and 3.50° E). The Bay of Palma is a nearly semi-circular and semi-enclosed basin located in the southwest coast of Mallorca and it can reach depths of more than 60 m. The Bay of Palma is defined as the water mass inside the square in Fig.1, consisting of a northern limit at $39°34'$N, a southern limit at $39°24'$N, and $2°30'$E and $2°45'$E as the western and eastern limits, respectively. The open boundary to the sea is in the southern part and it is 20 km wide.

The size of the Bay is smaller than the Rossby radius of deformation at these latitudes, and the main circulation is determined by the bathymetry at the bottom layer and by the wind and sea breeze at the surface layer. During summer there are persistent sea breeze conditions. In July and August, the weather is often almost identical from one day to the next. In the vicinity of the Bay and along the southern coast of Mallorca the breeze blows from the south-west. Several studies [33, 34], have pointed out that the meteorological conditions of Mallorca (intense solar radiation, clear skies, soil water deficit, dryness, weak surface pressure gradients, etc.) favors the development of sea breeze, often from April to October, and almost every day during July and August.

2.2 Data

The velocity data sets were obtained from the numerical model ROMS (Regional Ocean Model System). ROMS is a free surface, hydrostatic, primitive equation ocean model. The model uses a stretched, generalized nonlinear coordinate system to follow bottom topography in the vertical, and orthogonal curvilinear coordinates in the horizontal [36, 14]. At each grid point, horizontal resolution Δ_0 is the same in both the longitudinal, ϕ, and latitudinal, θ, directions.

We run the simulation with a resolution of $\Delta_0 = 0.0027°$ ($\sim 300m$, ROMS300), which is itself nested into a larger and coarser grid with $\Delta_0 = 1/74°$ ($\sim 1500m$). The ROMS300 domain covers 39°12′N - 39°36′N (latitude), and 2°24′E - 3°6′E (longitude). The total number of grid nodes is 260 × 148. Vertical resolution is variable with 10 layers in total. All domains were forced using realistic winds provided by the PSU/NCAR mesoscale model MM5. The initial vertical structure of temperature and salinity was obtained from the Levitus database [27, 1].

We will manage velocity data from the surface layer and the bottom layer for the grid of $\Delta_0 \approx 300m$. This domain allows us to analyze the fluid interchange between the Bay and the open ocean, using a high resolution velocity field. Vertical displacements between layers are neglected, which is justified by the small integration times we will use. Nevertheless, close to the coast they can have an impact that will be the subject of future work. We will study two different intervals of time: one starting on October 5th, 2008 and finishing on October 29th, 2008; and the other extends from July 1st, 2009 until July 26th, 2009. Temporal resolution is 15 minutes and 10 minutes for October and July, respectively, resulting in a total of 2375 snapshots of the velocity field for October, and 3744 for July.

3 Methodology

3.1 LCSs and particle dispersion from FSLE

Our methodology is based on the Lagrangian analysis of coastal flows. In the Lagrangian view, particles are advected by the flow and their horizontal motion (neglecting motions between model layers) is governed by the differential equations

$$\frac{dx}{dt} = v_x(x, y, t), \tag{1}$$

$$\frac{dy}{dt} = v_y(x, y, t), \tag{2}$$

where $(x(t), y(t))$ are the west-east and the south-north coordinates of the trajectories and (v_x, v_y) are the eastwards and northwards components of the velocity. Because of the small sizes involved, we will use a Cartesian coordinate system.

LCSs [15, 8, 35], are roughly defined as the material lines organizing the transport in the flow. They are the analogs, for time-dependent flows, of the unstable and stable manifolds of hyperbolic fixed points. Among other approaches [28, 29, 17], ridges of the local Lyapunov Exponents provide a convenient tool to locate them. In our case, we use the so-called Finite-Size Lyapunov Exponents (FSLEs) which are the adaptation of the asymptotic classical Lyapunov Exponent to finite spatial scales [2, 3]. Thus, they are specially suited for closed or semi-closed basins. FSLEs are a local measure of particle dispersion and thus of stirring and mixing, as a function of the spatial resolution, serving to isolate the different regimes corresponding to different length scales of the oceanic flows, very useful in coastal systems [7].

For any pair of fluid particles, one of them located at $\mathbf{x}$, the FSLE at time t_0 and at the spatial point $\mathbf{x}$ is given by the formula:

$$\lambda(\mathbf{x}, t_0, \delta_0, \delta_f) = \frac{1}{|\tau|} \ln \frac{\delta_f}{\delta_0}, \tag{3}$$

where δ_0 is the initial distance of the two given particles, and δ_f is their final distance. Thus, to compute the FSLEs we need to calculate the time, τ, needed for the two particles initially separated δ_0, to get a final distance δ_f (in this way the FSLE represents the inverse time scale for mixing up fluid parcels between length scales δ_0 and δ_f). To obtain this time we need to know the trajectories of the particles (from Eqs. (1) and (2)) which gives the Lagrangian character to this quantity. The FSLEs are computed for the points $\mathbf{x}$ of a lattice with lattice spacing coincident with the initial separation of fluid particles δ_0. Numerically we integrate the equations of motion using a standard, fourth-order Runge-Kutta scheme, with an integration time step of $dt = 15$ minutes in October and $dt = 10$ minutes in July. Since velocity information is provided just in a discrete space-time grid, spatiotemporal interpolation of the velocity data is achieved by bilinear interpolation. For the spatial scales that define FSLEs, we take $\delta_f = 0.1^\circ$, i.e., final separations of about 10 km, because of the size of the Bay. On the other side, we take δ_0 equals to 75 m, four times smaller than the resolution of the velocity field, $\Delta_0 = 300$ m. Since we are interested only in fast time scales, our integrations are restricted to 5 days. Locations for which the final separation at the end of this period has not reached the prescribed $\delta_f = 10$ km (or for which particles have been trapped by land) are assigned a value $\lambda = 0$.

FSLEs can be computed from trajectory integration *backwards* and *forwards* in time. Their highest values as a function of the initial location, $\mathbf{x}$, organize in filamental structures approximating relevant manifolds: ridges in the spatial distribution of backward (forward) FSLEs identify regions of locally maximum compression (separation), approximating attracting (repelling) material lines or unstable (stable) manifolds of hyperbolic trajectories, which can be identified with the LCSs [15, 8, 35, 38, 19], and characterize the flow from the Lagrangian point of view [21, 22]. Attracting LCSs associated to backward integration (the unstable manifolds) have a direct physical interpretation [21, 8, 9].

Tracers (chlorophyll, temperature, ...) spread along these attracting LCSs, thus creating their typical filamental structure [37, 24, 38, 6].

We close this section by noting that the relationship between LCSs and Lyapunov exponents is based on heuristic arguments which may not be correct in some cases (see for example [16]). The comparisons between FSLE and residence time maps presented later support the validity of the FSLE approach in the present situation.

3.2 Escape and residence times

Another characteristic time-scale for transport processes in open flows is the so-called escape rate [23]. This quantity measures how quickly particles trajectories escape from a domain. If we initiate $N(0)$ particles in a flow, we can measure how the trajectories escape the pre-selected region. In the case in which the decay in the number of particles remaining in the region up to time t, $N(t)$, decays exponentially with time, $N(t)/N(0) \sim e^{-\kappa t}$, there is a well defined escape time defined as the inverse of the escape rate κ: $\tau_e = 1/\kappa$. For the range of times explored in our work, we will see that the particle escape is close to exponential and then we can estimate the value of τ_e.

τ_e is a global quantity associated to the whole basin. A more detailed description of the transport processes can be obtained by other suitable Lagrangian quantities such as residence times [4, 5, 10, 31]. The particle residence time (RT) is defined as the interval of time that a fluid particle remains in a region before crossing a particular boundary. For each fluid particle inside the Bay at an initial time, we need to compute two times: the forward exit time, t_f, computed as the time needed for a particle to cross the line delimiting the Bay, taking the forward-in-time dynamics; and the backward exit time, t_b, the same but in the backward-in-time dynamics. The residence time is defined as $RT = t_f + t_b$. RTs can be displayed in plots named Lagrangian Synoptic Maps [26], in which the residence time of each fluid particle is referenced to its initial position on the grid.

4 Preliminary Eulerian description

A first approach to the transport process in the Bay can be a description from the Eulerian point of view, by studying averages of the velocity field. To do this we consider separately the meridional v_y and zonal v_x components of the surface flow, and we analyze the time evolution of their spatial averages.

Figures 2 a) and b) show the time series of data taken every 6 hours (solid line), and daily average time series (dashed-line) of v_x and v_y for October and July, respectively. During the two months both components of the flow present daily variability related to the presence of land and sea breezes. In July the meridional fluctuations are more noticeable, being $\langle v_y \rangle$ very small. In October there are some large fluctuations of low frequency, probably induced when the large-scale winds are variable.

Comparing the velocity components of both months we observe quantitative differences. The values of v_y in the case of October range from -0.6 to 0.6 m/s (bottom panel of Fig. 2 a), while in the case of July, v_y is two orders of magnitude smaller, ranging from -0.004 to 0.008 m/s (bottom panel of Fig. 2 b). On other hand, v_x are similar during October and July. In October, v_x ranges from -0.6 to 0.3 m/s (top panel of Fig. 2 a), the same order of magnitude than the meridional velocity, resulting in circular motions (clockwise along the Bay). In July the situation is significantly different. The zonal velocity ranges from -0.8 to 0.2 m/s (top panel of Fig. 2 b), much larger than the meridional velocity, resulting in a flow dominated by the zonal component.

5 Lagrangian Results

5.1 Average characterization of stirring

We now describe the Lagrangian results. First we compute the temporal average (over the months of October and July) of the FSLEs for the surface layer, and for July in the bottom layer. This calculation helps us to unveil areas of different stirring and the differences between layers and months.

The surface computations for the different seasonal months, October and July (Fig. 3 a, b) show different values and spatial distributions of stirring. The Bay of Palma appears to be an area with important activity. Average FSLE field looks more homogeneous in July than in October. During October filamental structures of high values of FSLE are accumulated over the northeast side of the Bay, forming a linear structure running from north to south-east which can act as a barrier, and therefore dividing the Bay in two flow regions of qualitatively different dynamics. The response of the surface currents to forcing by the wind could be an explanation of the difference between seasons. The effect of the terrain topography on stirring is clear in Fig. 3 c), where FSLEs are computed at the deepest layer for July. The high values of time-averaged FSLEs are located close to a region of high bathymetry gradient. This feature is likely owing to the presence of a region of compression of the flow induced by the bathymetry.

5.2 Coastal LCSs

The temporal averages computed in Sec. 5.1 give us a rough idea of stirring in the Bay. More detailed information is obtained by looking at non-averaged quantities, that may reveal the existence of barriers to transport. Figure 4 shows the location of the high backward FSLE values (LCSs), appearing as a network of lines, computed at successive instants of time in October. These temporary structures can remain for one or more days, as happens in October, or they can appear in the same location periodically (not shown). We stress here the appearance of a clear barrier, from north to south-east, that divides the Bay in two areas that correlates with the temporal average in Fig. 3 a). This barrier appears in almost the same position in different days, remaining without displacing too much. To effectively see that it acts as a barrier we have considered the evolution of virtual particles released at both sides of the barrier. Red and black particles do not mix and they tend to spread along the barrier (confirming that, as expected, it is an attracting line).

5.3 Transport between the Bay of Palma and the open sea

In this section we study the surface transport of particles in and out of the Bay. To have an idea of the time scales involved in this interchange we proceed by computing the number of particles remaining in the Bay, $N(t)$, averaged over different starting times (separated by 18hours in order to collect the information of diurnal and nocturnal signal; this gives us 15 different simulations to be averaged for each month) as a function of the integration time t. A particle is considered to leave the Bay when crossing the red open-sea boundary in Fig. 1, so that particles landing on the coast are considered not escaped. Fig. 5 shows the different average decays for October and July. In both cases $N(t)$ is reasonably fitted by an exponential in the considered time-range, thus identifying the escape rates $\kappa = 0.62$ and 0.47 $days^{-1}$, respectively. The corresponding escape times, given by the inverse of the escape rate, are, respectively, $\tau_e = 1.61$ and 2.12 $days$. The exchange of fluid particles between the open ocean and the Bay is then less active in summer than in autumn.

Next we compute synoptic maps of the residence times. As was indicated in Sec. 3.2 the residence time of the particles throughout the study area is considered as the sum of the entry time (t_b) and the escape time (t_f). To compute t_f and t_b particles are initialized every 6 hours in a regular grid of $75m$ spacing and they are integrated forward and backward in time during 5 days. We consider that 5 days is a proper integration time according with the time scales associated with the coastal processes of this small Bay, and also owing to the short period of the available data. In these computations we assign the maximum possible value of t_f and t_b (5 days) to the fluid particles that remain in the pre-selected area after the 5 days of integration.

In Fig. 6 we color the initial positions of particles in the Bay attending to the time they transit through the Bay ($RT = t_f + t_b$) for different days. Initial positions of particles with short residence times are indicated in blue in Fig. 6. Regions from where particles have longer residence time (i.e. take more time between entry and escape) are marked in red/brown.

These maps show that the spatial distribution of residence times of particles can be complex and time depending, presenting different patterns at different times. A number of small structures can be observed, including thin filaments or small lobes. Comparing both months, one can see differences in the RT distributions. The most noticeable is the approximate east-west alignment of the zones of similar RT in July, which is not seen in October. Also, in October the values of residence times of the particles are smaller, in agreement with the global rate estimations showed before. A common feature is the southwest region with low values of residence times, because in this region there are not coastal boundaries and it is totally open to the ocean.

In order to reveal regions with different persistent transport properties we compute time averages of the spatial distributions of residence times. We average 6-hourly snapshots of RT during 15 days (i.e. 60 snapshots) for each month. The results, plotted in Fig. 7 a) and b), show the common features that, in general, the low values of RT are for particles initiated close to the open ocean, specially in the southwest part, and high values are for particles started near the coast, as expected. However, on average, the residence time is larger in July than in October (3.25 days in July and 1.51 days in October) consistent with the behavior of the corresponding values of τ_e. Also, in July there is a clear boundary between the interior of the Bay to the north, with large average residence times and the open sea to the south, whereas the boundary between high and low residence times in October is well inside the Bay, aligned with the Lagrangian structure identified from the FSLE analysis, as will be discussed in the next section.

Another feature observed in movies of particle trajectories (not shown) is that in October fluid particles tend to circulate mostly clockwise, while in July they are oscillating along the zonal direction (see Section 4). This difference is likely to be responsible for the different behavior between both months.

5.4 Relation between LCSs and RTs

We now examine the connection between regions of different residence times with LCSs. To compare RT and FSLE we have superimposed in Fig. 6 the filaments of high values of forward (white) and backward FSLE (black) values on the spatial distribution of residence times. This Figure shows a clear correspondence between structures of RT and FSLE. The LCSs given by high values of FSLE clearly separate regions with different values of residence times, confirming the value of the FSLE technique to identify boundaries between different flow regions and barriers to transport. [32] studied the relation between residence time and FSLE for a wind-forced hydrodynamical model of a shallow lake. They found that areas with long residence time visualize the stable manifolds of the so-called chaotic saddle, a structure controlling the escape properties at long times. In our case, our integrations are restricted to times too short to characterize long-time chaotic behavior, but still there is a good correspondence between the FSLE structures characterizing divergent or convergent trajectories, and escape or residence times.

Fig. 7 a) shows a time average over October of the spatial distribution of RT, to be compared with the corresponding average figure (Fig. 3 a) for FSLE. It is evident that the region in the north and east side of the Bay with high values of RT is separated from the rest by a region of high values of FSLE. This can be explained by the presence of persistent barriers which do not allow particles to escape from the northeast side of the Bay, and thus separating the Bay in regions with different residence times. In July the situation is different, because the spatial distribution of FSLE (Fig.3 b) and RT (Fig. 7 b) is almost homogeneous, with higher values over the whole area of the Bay, and lower values in the small region bordering the open ocean. Nevertheless, the instantaneous configurations of high FSLE lines (Fig. 6) reveal their general east-west alignment, consistent with the orientation of the boundaries between areas of different RTs.

5.5 Variability of RT and FSLE

The differences of residence times and FSLEs in the two considered months indicate that the dynamics of the flow is qualitatively different. Now we analyze the time evolution of their spatial averages.

Figures 8 a) and b) show the time series of the spatial mean of residence times (top panel) and FSLE (bottom panel) for October and July, respectively.

Comparison between time evolution of spatial average of the RT for the different months confirms, again, that particles tend to stay longer times in the Bay during July than in October. The values of RT vary approximately from 0.25 days to 3 days in October (Fig. 8 a, top), and from 2 days to 6 days in July (Fig. 8 b, top). The same happens with FSLE, higher values correspond to July and lower ones to October. Diurnal fluctuations, likely related to the effect of the sea breeze, are evident in RT and FSLE for both months.

In October there are some large fluctuations of low frequency in RT, probably induced by the variability of remote forcing winds. On the other hand, during October, minima of RT correspond to maxima of FSLE, and maxima of RT correspond to minima of FSLE. In July, the relationship between FSLE and RT is looser and only observed in the high-frequency fluctuations. This difference in behavior probably arises from the fact that high values of FSLE determine clear and well-defined barriers to transport only in the case of October (see Sect. 5.3 and 5.4). In July lines of high FSLE remain nearly horizontal and probably represent regions of high zonal shear everywhere in the Bay, that by themselves do not imply stronger or weaker escape towards the South.

5.6 Transport at the bottom layer

In this subsection we compare the main Lagrangian characteristics at the bottom layer, not driven directly by wind, with those at the surface. In Fig. 9 a) we show an instantaneous map of the residence times in the bottom layer one day of July, overlayed with lines of high FSLE values. Again, the spatial distribution is inhomogeneous, and we find high values of RT over all the Bay except very close to the ocean. The correlation of RT values with FSLE lines is weaker than in the upper layer, but still we see that the relatively lower values of RT in the western part of the Bay at that particular day appear bounded by backwards FSLE lines, indicating a temporal escape route of particles in that region towards the southwest. The spatial distribution of the time average of RT plotted in Fig. 9 b) shows that highest average values of RT are concentrated in the northwestern region of the Bay. Fig. 3 c) displays high values of FSLE located precisely in the same region where the RT qualitatively change to high values. This suggests the presence of persistent barriers that separate this southeastern region from the rest in this bottom layer. The formation of these persistent LCSs is, probably, produced by the gradient of the bathymetry (see Fig. 1).

The time evolution of the spatial average of RT and FSLE are plotted in top and bottom panel of Fig. 10 respectively. Contrarily to the surface, in the bottom layer the diurnal fluctuations in the time series of RT disappear, showing that the flow at this depth is not directly influenced by breeze. The RT values are larger than in the surface, and therefore the interchange between the ocean and the Bay is less intense at bottom layers. This is a consequence of the smoothness of the flow produced by the absence of the wind forcing at deepest levels. In average, there is a negative relation between stirring and residence times: when the flow is more dispersive the particles transit during less time over the Bay, so that maxima of RT correspond to minima of FSLE and vice-versa.

6 Conclusions.

Properties of coastal transport in the Bay of Palma, which is a small semi-enclosed region of the Island of Mallorca, were studied in a Lagrangian framework, by using a realistic model velocity data at high resolution. We have applied two Lagrangian methods (FSLEs and RT) to analyze the small scales of these coastal currents. LCSs have been detected as ridges of FSLE, and virtual experiments with particle trajectories have shown that these structures really act as barriers, organizing the coastal flow. Global and average aspects of the transport in different seasonal months show that, in the period studied, in autumn there is more interaction between the Bay and the open ocean than in summer. One explanation is that during July the flow conditions restrict motion of the coastal marine surface to the zonal direction, preventing the flow to enter or scape toward the open ocean. The transport of particles at the deepest layer, strongly influenced by the bottom topography, is less active than at the surface. Regions with different values of RT are separated by ridges of FSLE, proving the fact that FSLE separate regions of qualitatively different dynamics also in small coastal regions. Thus, we think that these Lagrangian quantities can be used as key variables determining the dynamics and health of other bays or estuaries, particularly in relation with human activities. Future improvements include the adaptation of these methods to three-dimensional spaces and capture three-dimensional effects, such as upwelling and downwelling in coastal areas, and analyzing longer periods of time.

Acknowledgments

I.H-C, C.L and E.H-G acknowledge support from MICINN and FEDER through projects FISICOS (FIS2007-60327), INTENSE@COSYP (FIS2012-30634), and ESCOLA (CTM2012-39025-C02-01). AO acknowledges financial support from MICINN and EU-Med Programme through projects BUS2 (CGL2011-22964) and TOSCA (2GMED-09-425). We acknowledge the ICMAT Severo Ochoa project (SEV-2011-0087) for the funding of the publication charges of this article.

References

[1] J. I. Antonov, R. A. Locarnini, T. P. Boyer, A. V. Mishonov, and H. E. Garcia. *World Ocean Atlas 2005, Volume 2: Salinity. S. Levitus, Ed. NOAA Atlas NESDIS 62.* U.S. Government Printing Office, Washington, D.C, 2006.

[2] E. Aurell, G. Boffetta, A. Crisanti, G. Paladin, and A. Vulpiani. Predictability in the large: an extension of the Lyapunov exponent. *J. Phys. A*, 30:1–26, 1997.

[3] G. Boffetta, G. Lacorata, G. Redaelli, and A. Vulpiani. Detecting barriers to transport: a review of different techniques. *Physica D*, 159:58–70, 2001.

[4] G. Buffoni, A. Cappelletti, and E. Cupini. Advection-diffusion processes and residence times in semi-enclosed marine basins. *Int. J. Numer. Methods Fluids*, 22:1–23, 1996.

[5] G. Buffoni, P. Falco, A. Griffa, and E. Zambianchi. Dispersion processes and residence times in a semi-enclosed basin with recirculating gyres: an application to the Tyrrhenian Sea. *J. Geophys. Res*, 102(C8):18699–18713, 1997.

[6] P. Calil and K.J. Richards. Transient upwelling hot spots in the oligotrophic North Pacific. *J. Geophys. Res*, 115:C02003, 2010.

[7] M. Cencini, F. Cecconi, and A. Vulpiani. Chaos: From simple models to complex systems. *Series on Advances in Statistical Mechanics, World Scientific,*, 2010.

[8] F. d'Ovidio, V. Fernández, E. Hernández-García, and C. López. Mixing structures in the Mediterranean sea from finite-size Lyapunov exponents. *Geophys. Res. Lett.*, 31:L17203, 2004.

[9] F. d'Ovidio, J. Isern-Fontanet, C. López, E. Hernández-García, and E. García-Ladona. Comparison between Eulerian diagnostics and Finite-Size Lyapunov Exponents computed from altimetry in the Algerian basin. *Deep-Sea Res. I*, 56:15–31, 2009.

[10] P. Falco, A. Griffa, and P. M. Poulain. Transport properties in the Adriatic Sea as deduced from drifter data. *J. Phys. Oceanogr.*, 30(8):2055–2071, 2000.

[11] L. A. Fiorentino, M. J. Olascoaga, A. Reniers, Z. Feng, F. J. Beron-Vera, and J. H. MacMahan. Using Lagrangian Coherent Structures to understand coastal water quality. *Continental Shelf Research*, 47:145–149, 2012.

[12] A. Galan, A. Orfila, G. Simarro, I. Hernández-Carrasco, and C. López. Wave mixing rise inferred from Lyapunov exponents. *Environmental Fluid Mechanics*, 12:291–300, 2012.

[13] H. Gildor, E. Fredj, J. Steinbuck, and S. Monismith. Evidence for Submesoscale Barriers to Horizontal Mixing in the Ocean from Current Meauserements and Aerial Photographs. *Journal od Physical Oceanography*, 39:1975–1983, 2009.

[14] D. E. Haidvogel, J. Blanton, J. C. Kindle, and D. R. Lynch. Coastal Ocean Modeling: Processes and Real-Time Systems. *Oceanography*, 13(1):35–46, 2000.

[15] G. Haller and G. Yuan. Lagrangian coherent structures and mixing in two-dimensional turbulence. *Physica D*, 147:352–370, 2000.

[16] G. Haller. A variational theory of hyperbolic Lagrangian coherent structures. *Physica D*, 240(7):574 – 598, 2011. Erratum and addendum: Physica D 241, 439–441 (2012).

[17] G. Haller and F. J. Beron-Vera. Geodesic theory of transport barriers in two-dimensional flows. *Physica D: Nonlinear Phenomena*, 241(20):1680 – 1702, 2012.

[18] A. C. Haza, T. M. Özgökmen, A. Griffa, A. Molcard, P. M. Poulain, and G. Peggion. Transport properties in small-scale coastal flows: relative dispersion from VHF radar measurements in the Gulf of La Spezia. *Ocean Dynamics*, 60:861–882, 2010.

[19] I. Hernández-Carrasco, C. López, E. Hernández-García, and A. Turiel. How reliable are finite-size Lyapunov exponents for the assesment of ocean dynamics? *Ocean Modelling.*, 36(3-4):208–218, 2011.

[20] F. Huhn, A. von Kameke, S. Allen-Perkins, P. Montero, A. Venancio, and V. Pérez-Muñuzuri. Horizontal Lagrangian transport in a tidal-driven estuary –transport

barriers attached to prominent coastal boundaries. *Continental Shelf Research.*, 39-40:1–13, 2012.

[21] B. Joseph and B. Legras. Relation between Kinematic Boundaries, Stirring, and Barriers for the Antartic Polar Vortex. *J. Atm. Sci.*, 59:1198–1212, 2002.

[22] T. Koh and B. Legras. Hyperbolic lines and the stratospheric Polar vortex. *Chaos*, 12(2):382–394, 2002.

[23] Y. C. Lai and T. Tel. *Transient Chaos: Complex Dynamics on Finite-Time Scales.* Springer, 2011.

[24] Y. Lehan, F. d'Ovidio, M. Lévy, and E. Heyfetz. Stirring of the Northeast Atlantic spring bloom: A Lagrangian analysis based on multisatellite data. *J. Geophys. Res.*, 112:C08005, 2007.

[25] F. Lekien, C. Coulliette, A. J. Mariano, E. H. Ryan, L. K. Shay, G. Haller, and J. Marsden. Pollution release tied to invariant manifolds: A case study for the coast of Florida. *Physica D.*, 210:1–20, 2005.

[26] B. L. Lipphardt, Jr., D. Small, A. D. Kirwan, Jr., S. Wiggins, K. Ide, C. E. Grosch, and J. D. Paduan. Synoptic lagrangian maps: Aplication to surface transport in Monterey Bay. *Journal of Marine Research*, 64:221–247, 2006.

[27] R. A. Locarnini, A. V. Mishonov, J. I. Antonov, T. P. Boyer, and H. E. Garcia. *World Ocean Atlas 2005, Volume 1: Temperature. S. Levitus, Ed. NOAA Atlas NESDIS 61.* U.S. Government Printing Office, Washington, D.C, 2006.

[28] A. M. Mancho, D. Small, and S. Wiggins. A tutorial on dynamical systems concepts applied to lagrangian transport in oceanic flows defined as finite time data sets: Theoretical and computational issues. *Physics Reports*, 437(34):55 – 124, 2006.

[29] C. Mendoza and A. M. Mancho. Hidden geometry of ocean flows. *Phys. Rev. Lett.*, 105:038501, Jul 2010.

[30] J. C. Ohlmann, J. H. LaCasce, L. Washburn, A. J. Mariano, and B. Emery. Relative dispersion observations and trajectory modeling in the Santa Barbara Channel. *J. Geophys. Res.*, 117:C05040, 2012.

[31] A. Orfila, A. Jordi, G. Basterretxea, G. Vizoso, N. Marba, C. M. Duarte, F. E. Werner, and J. Tintoré. Residence time and posidonia oceanica in Cabrera Archipelago National Park, spain. *Continental Shelf Research*, 25:1339–1352, 2005.

[32] M. Pattantyús-Ábrahám, T. Tél, T. Krámer, and J. Józsa. Mixing properties of a shallow basin due to wind-induced chaotic flow. *Advances in Water Resources*, 31:525–534, 2008.

[33] C. Ramis and S. Alonso. Sea Breeze convergence line in Mallorca. a satellite observation. *Weather*, 43:288–293, 1988.

[34] C. Ramis and R. Romero. A First Numerical Simulation of the Development and Structure of the Sea Breeze in the Island of Mallorca. *Ann. Geophy.*, 13:981–994, 1995.

[35] S. C. Shadden, F. Lekien, and J. E. Marsden. Definition and properties of lagrangian coherent structures from finite-time lyapunov exponents in two dimensional aperiodic flows. *Physica D*, 212:271–304, 2005.

[36] Y. Song and D. Haidvogel. A Semi-implict Ocean Circulation Model Using a Generalized Topography-Following Coordinate System. *Journal of Computational Physics*, 115(1):228–244, 1994.

[37] T. Tel and M. Gruiz. *Chaotic Dynamics- An Introduction Based on Classical Mechanics*. Cambridge University Press, Cambridge, 2006.

[38] E. Tew Kai, V. Rossi, J. Sudre, H. Weimerskirch, C. López, E. Hernández-García, F. Marsac, and V. Garçon. Top marine predators track Lagrangian coherent structures. *Proceedings of the National Academy of Sciencies of the USA*, 106:8245–8250, 2009.

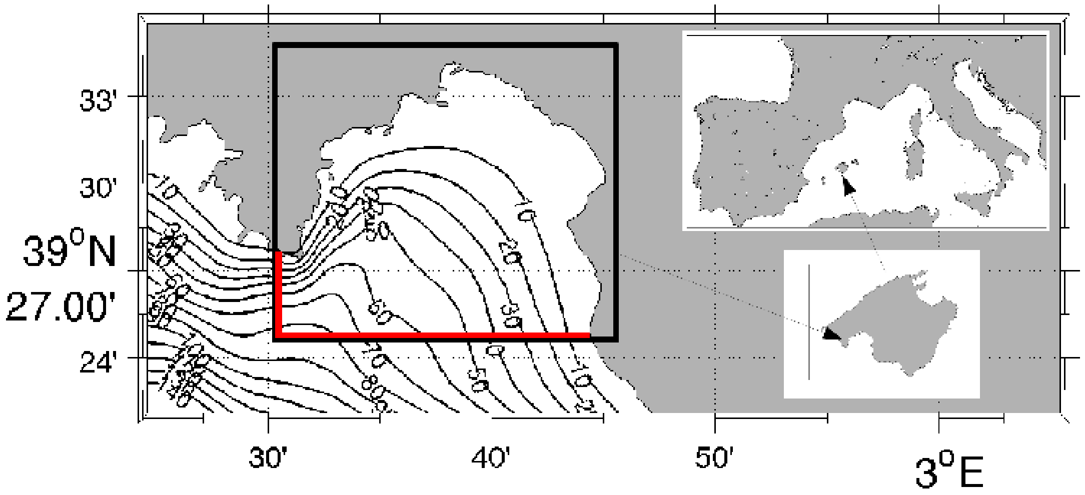

Figure 1: Bathymetry contours (in meters) of the model domain. The black box indicates the Palma Bay and the inset graphics give the geographical location of Mallorca Island in the western Mediterranean Sea.

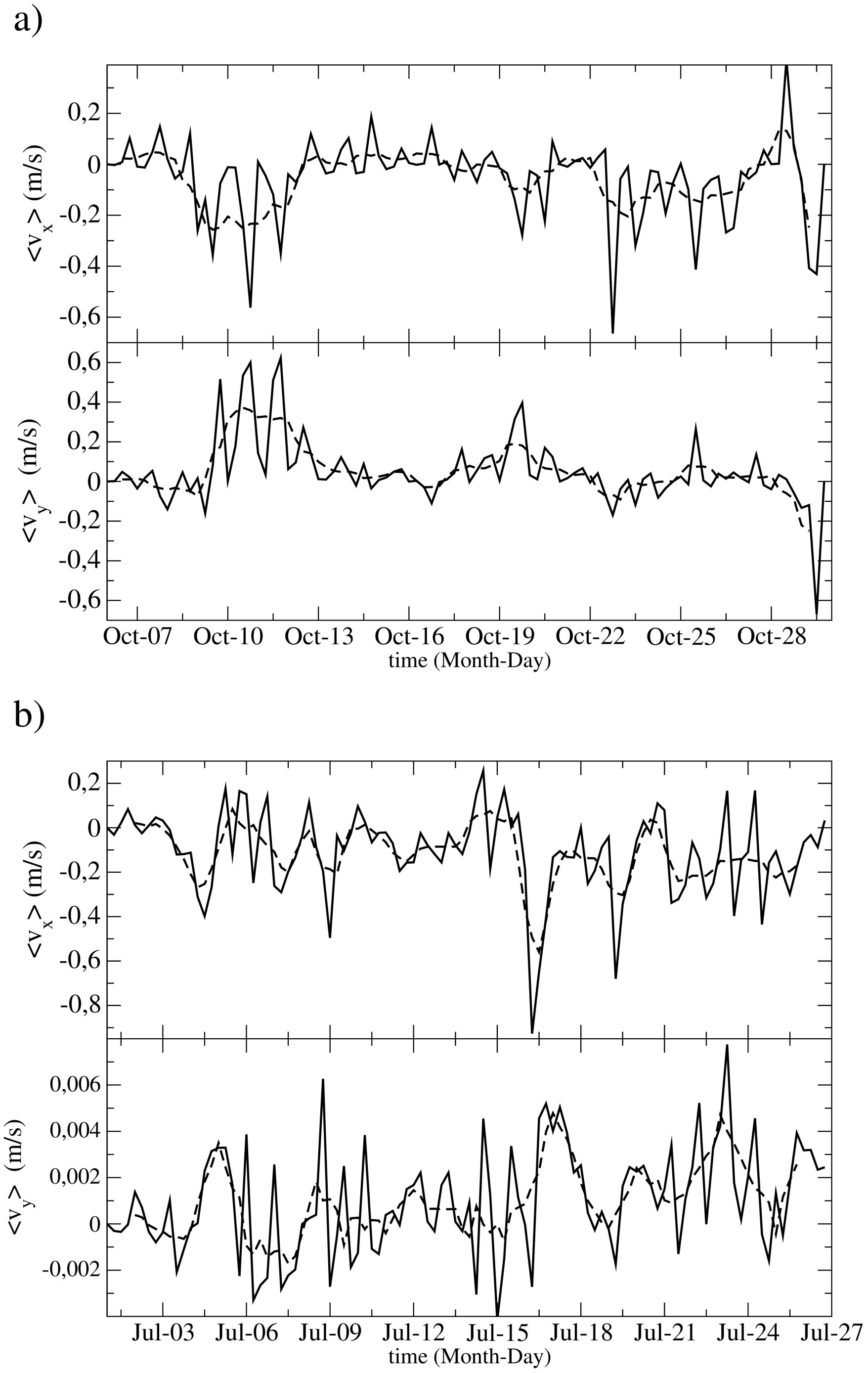

Figure 2: a) Time series throughout October of the zonal (top) and meridional (bottom) components of the velocity field every 6 hours (solid line) and daily averaged (dashed-line); b) the same that a) but for July.

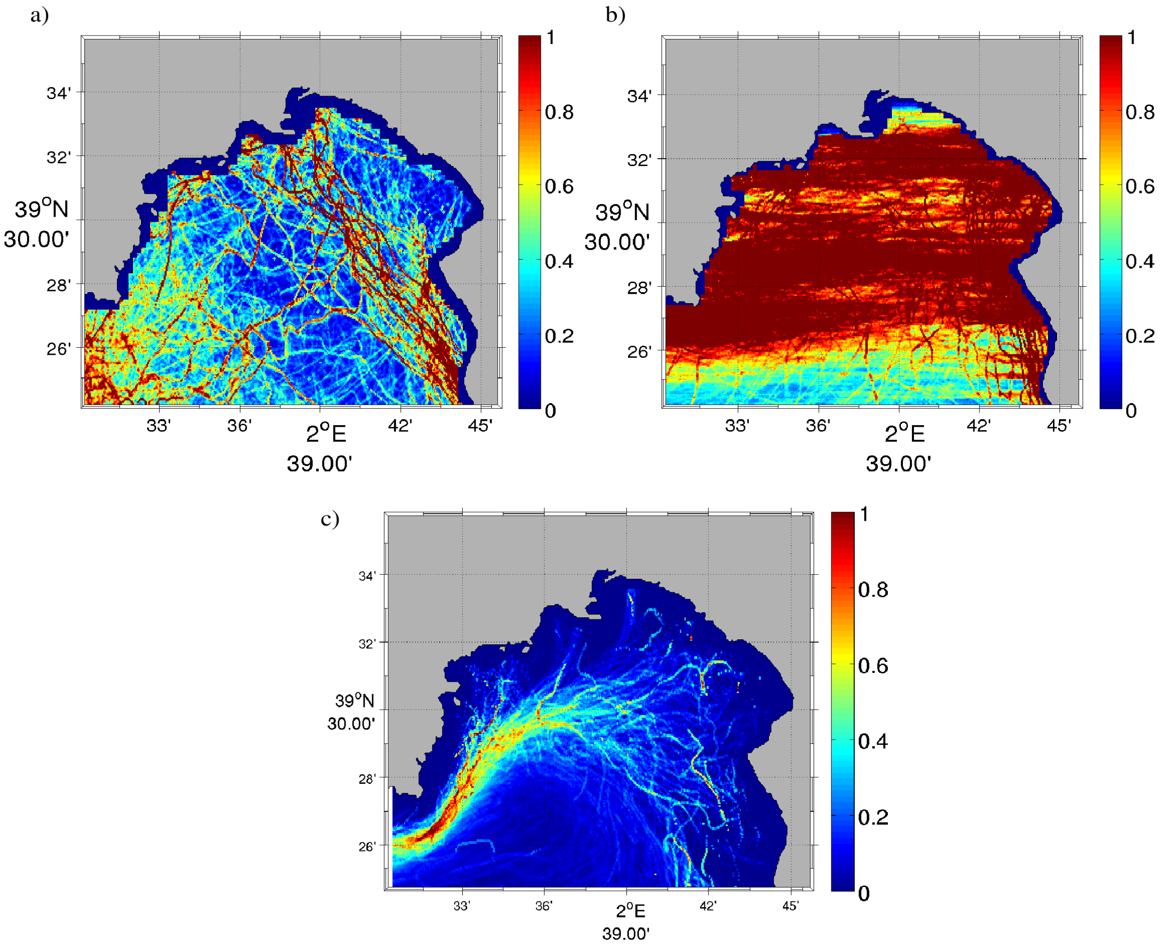

Figure 3: Spatial distribution of the time average of 6-hourly FSLEs maps over different months and at different layers: a) October at surface layer, b) July at surface layer, c) July at bottom layer.

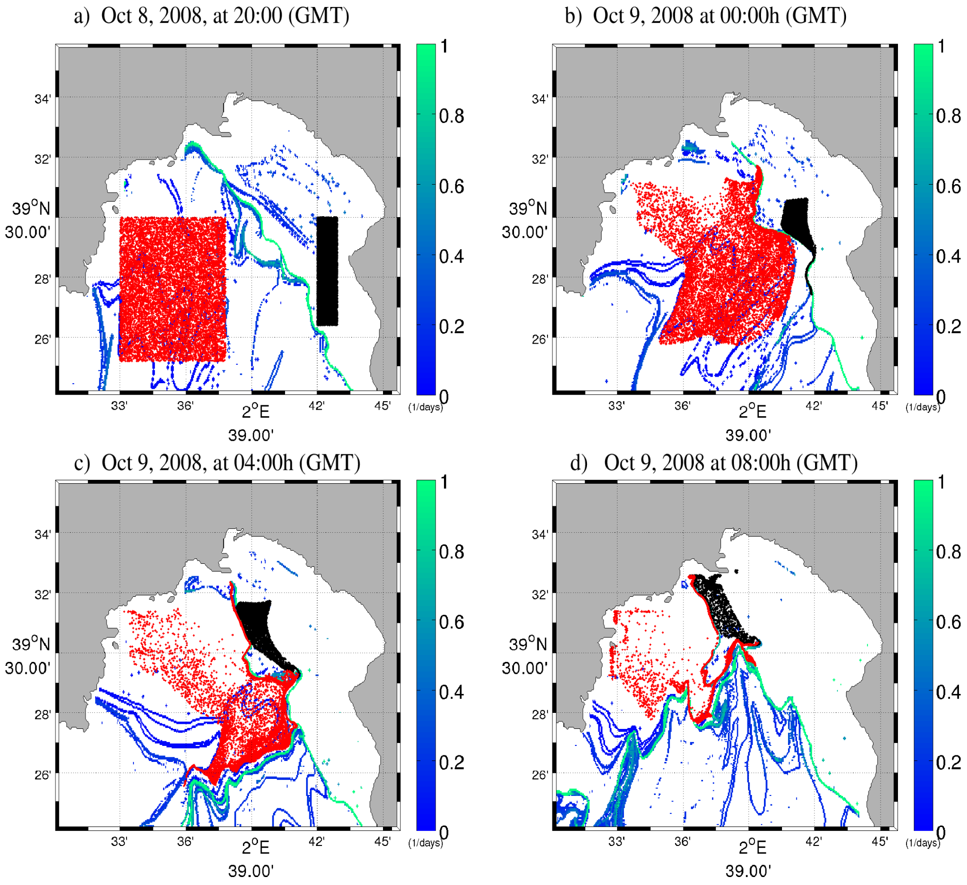
a) Oct 8, 2008, at 20:00 (GMT)

b) Oct 9, 2008 at 00:00h (GMT)

c) Oct 9, 2008, at 04:00h (GMT)

d) Oct 9, 2008 at 08:00h (GMT)

Figure 4: Evolution of the locations of two sets of particles in the Palma Bay during a night of October, superimposed on the spatial distributions of high values of backward FSLEs. The colorbars specify FSLE values in days^{-1}. Zero FSLE values, displayed as white, are assigned to locations for which the particles do not attain the prescribed $\delta_f = 10km$ separation after 5-days integration. Note the highest values of FSLEs (green lines) act as a barrier practically dividing the Bay in two parts. The two sets of particles are deployed from both sides of the barrier. (a) Initial conditions of the particles on October 8 at 20:00 GMT, 2008.; (b) October 9 at 00:00 GMT, 2008 ; (c) October 9 at 04:00 GMT, 2008 ; (d) October 9 at 08:00 GMT, 2008. Particles marked by black dots were released in the right side (northeast) of the barrier while the particles marked with red were released on the left side of the barrier.

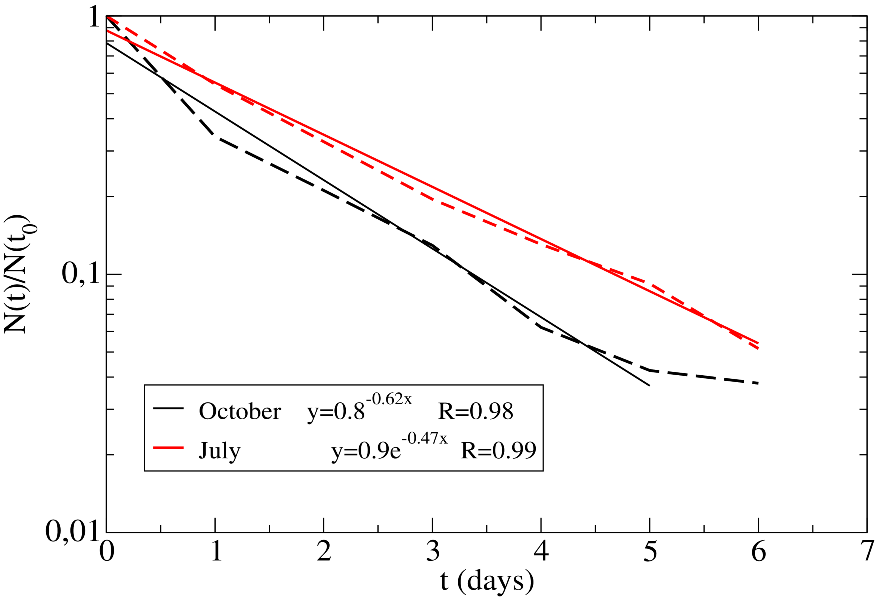

Figure 5: Average of 15 subsequent (started at t_0 values separated 18 hours) estimations of $N(t)$, the number of particles remaining in Palma Bay at least for a lapse of time t after release at t_0. Black and red lines are for surface layer in October and July respectively. Dashed lines are the measured averages, and the solid lines are the indicated exponential fits.

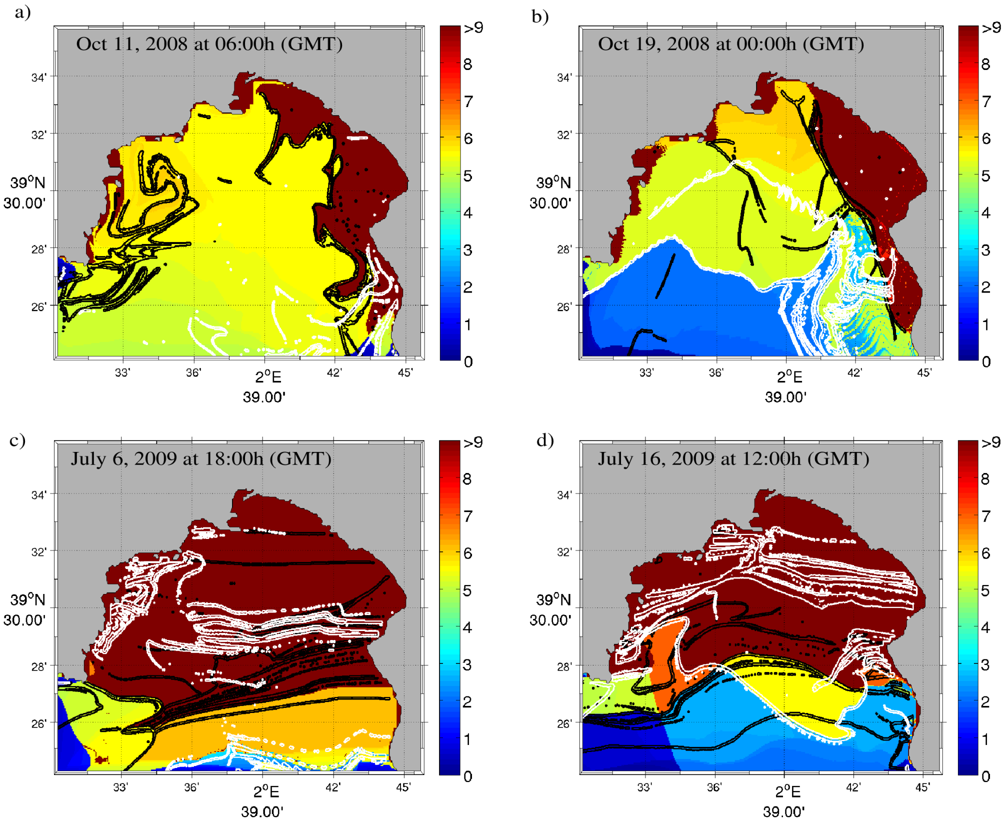
a)
Oct 11, 2008 at 06:00h (GMT)
b)
Oct 19, 2008 at 00:00h (GMT)
c)
July 6, 2009 at 18:00h (GMT)
d)
July 16, 2009 at 12:00h (GMT)
34'
32'
39°N
30.00'
28'
26'
33'
36'
2°E
39.00'
42'
45'
>9
8
7
6
5
4
3
2
1
0

Figure 6: Lines are the locations of top values of FSLE (greater than $0.5 days^{-1}$ in October and greater than $1.5 days^{-1}$ in July). Backward FSLE lines are colored in black and forward FSLEs in white. They are superimposed on spatial distributions of residence times in Palma Bay for different dates. The colorbars give the residence times in days. a) and b) correspond to two different days in October, and c) and d) in July.

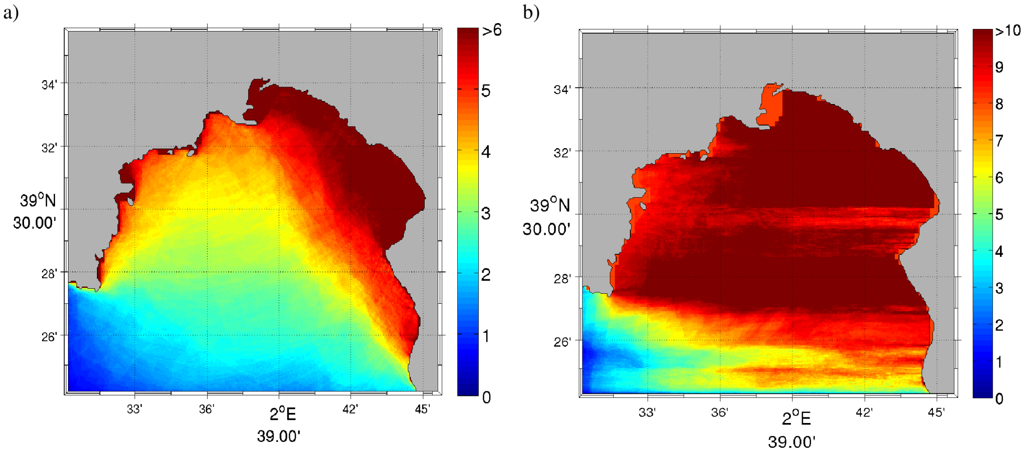

Figure 7: Spatial distributions of time averages of 60 snapshots of 6-hourly RT values collected over 15 days in Palma Bay for a) October and b) July. The colorbar units are *days*.

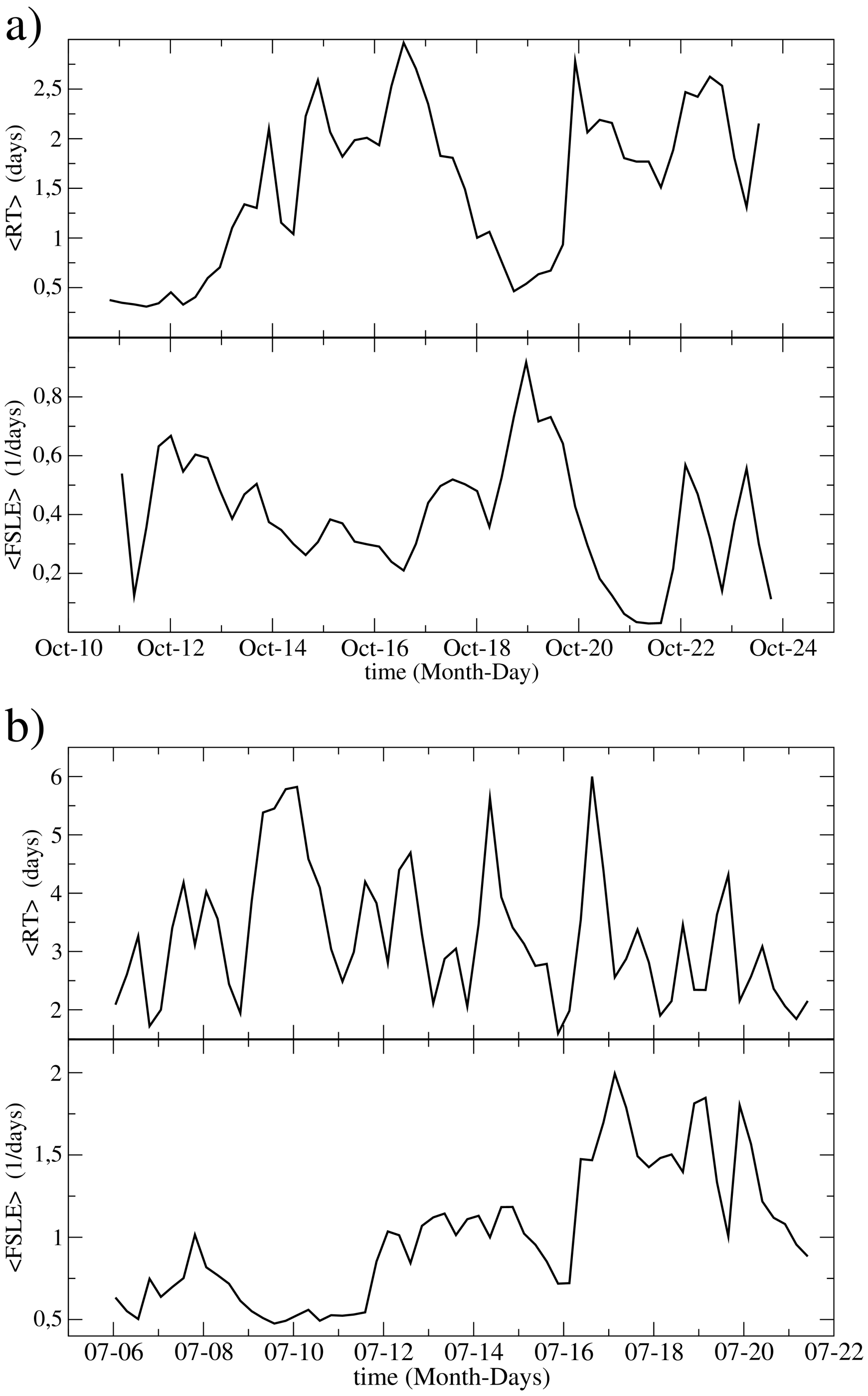

Figure 8: a) Time series throughout October of the spatial average of residence times (top) and spatial average of FSLE (bottom) for the surface layer of Palma Bay. b) the same that a) but for July.

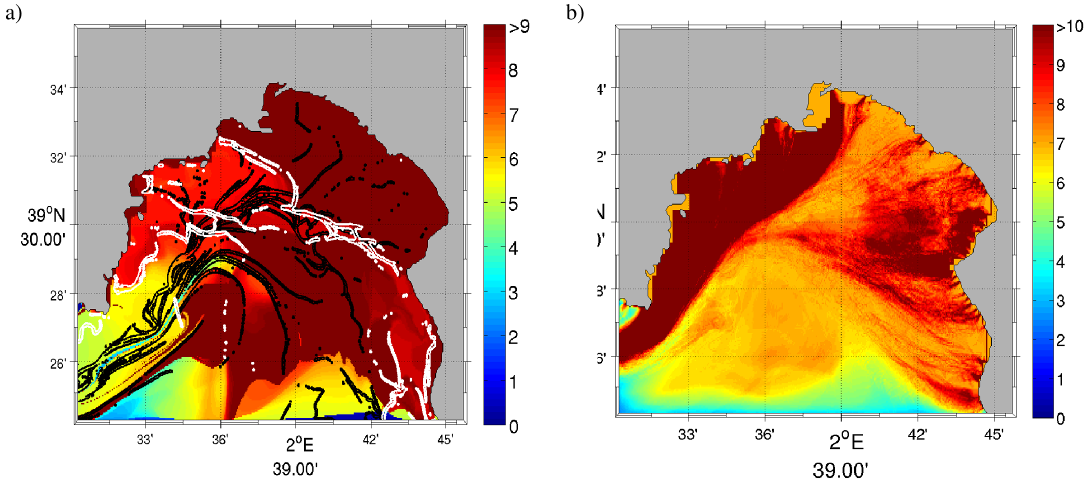

Figure 9: a) Snapshot of spatial distributions of residence times at the bottom layer in Palma Bay corresponding to July 17, 2009 at 18:00h (GMT). Lines are the locations of top values of FSLE (greater than $0.3 days^{-1}$). Backward FSLE lines are colored in black and forward FSLEs in white. b) spatial distribution of time average of 60 snapshots of 6-hourly maps of RT collected over 15 days in July at the bottom layer.

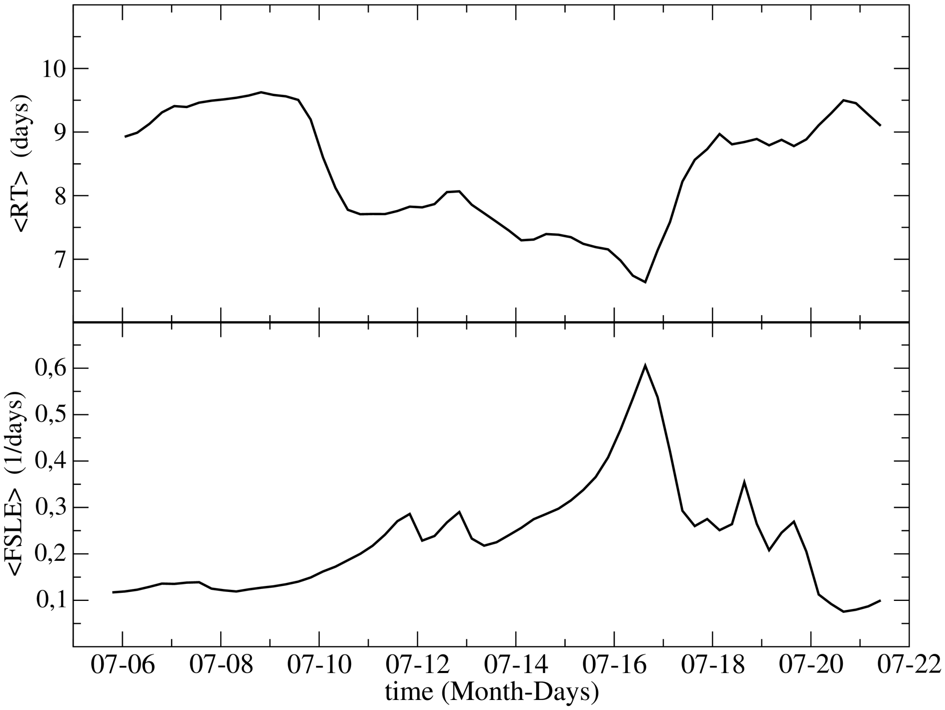

Figure 10: Time series throughout July of (top) spatial average of residence times and (bottom) spatial average of FSLE computed for the bottom layer.